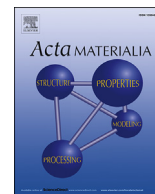




Contents lists available at ScienceDirect

Acta Materialia

journal homepage: www.elsevier.com/locate/actamat

Full length article

Microstructure and mechanical properties of nucleant-free Li₂O-CaO-SiO₂ glass-ceramics

Gisele G. Santos^{a,*}, Francisco C. Serbena^b, Vladimir M. Fokin^{a,c}, Edgar D. Zanotto^a^a Vitreous Materials Laboratory, Department of Materials Engineering, Federal University of São Carlos (UFSCar), 13565-905, São Carlos, SP, Brazil^b Department of Physics, State University of Ponta Grossa (UEPG), 84.030-900 Ponta Grossa, PR, Brazil^c Vavilov State Optical Institute, ul. Babushkina 36-1, 193171 St. Petersburg, Russia

ARTICLE INFO

Article history:

Received 10 November 2016

Received in revised form

4 March 2017

Accepted 6 March 2017

Available online xxx

Keywords:

Crystallization

Glass-ceramic

Mechanical property

Lithium metasilicate

Wollastonite

ABSTRACT

An attractive characteristic of the Li₂O-CaO-SiO₂ glass-forming system is the possibility of obtaining internally nucleated crystal phases – CaSiO₃ and Li₂SiO₃ – having elongated morphologies that can potentially lead to tough glass-ceramics. Another great advantage of this system is that it does not need a nucleating agent to crystallize internally. In this research work, three glasses with systematic compositional variations within the range of 30–50 mol% CaSiO₃/70–50 mol% Li₂SiO₃ were prepared, heat-treated and their microstructures and mechanical properties evaluated. Heating cycles were applied in two-stage treatments. The temperatures were selected based on previous DSC analyses. The crystallized samples were characterized by XRD and SEM to examine the nature, size and morphology of their crystals. The effect of microstructure on the Vickers hardness (H_V) and indentation fracture toughness (K_{IC}) of the glass-ceramics was determined. Elastic modulus (E), biaxial strength (σ_m) and fracture toughness (K_{DTIC}) were determined from nanoindentation, ball-on-three-balls and double torsion tests, respectively. The level of internal residual stresses was evaluated by X-rays diffraction. The best mechanical properties were exhibited by a composition containing 44 mol% CaSiO₃ heat-treated at 498 °C for 24 h for nucleation and at 700 °C for 2 h for crystal growth. This composition resulted in a glass-ceramic with the following microstructural features and properties: average Li₂SiO₃ (LS) crystal size of 8.5 μm , wollastonite (CS) phase surrounding the LS crystals with approximately 50% LS crystallized volume fraction, $K_{DTIC} = 2.3 \pm 0.5 \text{ MPa m}^{1/2}$, $\sigma_m = 270 \pm 20 \text{ MPa}$, $H_V = 8.4 \pm 0.7 \text{ GPa}$ and $E = 146 \pm 8 \text{ GPa}$. These are exciting mechanical properties for glass-ceramics intended for load bearing applications.

© 2017 Acta Materialia Inc. Published by Elsevier Ltd. All rights reserved.

1. Introduction

Glass-ceramics are polycrystalline materials produced through the controlled internal crystallization of certain glasses, and contain one or more crystalline phases embedded in a residual glass phase. These materials are obtained by subjecting the parent glass to controlled heat treatments that favor internal nucleation followed by crystal growth [1]. The advantages of glass-ceramics over sintered ceramics is their negligible or even zero porosity, easier microstructural design and control, greater uniformity, possibility of rapidly producing complex shapes using fast glass-forming techniques, and reproducibility [2]. The chemical composition influences their glass forming ability, their ability for nucleus

formation and growth, and the nature of their crystal phase, while the microstructure is a key factor for most properties [3].

With respect to mechanical properties, the performance of glasses is usually inferior to that of ceramics. However, this disadvantage is overcome by the possibility of designing and producing pore-free glass-ceramic microstructures that enable the development of new materials with unusual combinations of properties. Therefore, the study of the crystallization behavior of glass-forming systems and the evaluation of their properties epitomize a significant field in glass technology for developing new materials and products [4]. As a matter of fact, a recent study by Mauro and Zanotto [5] demonstrated that the most frequent keyword in the past 200 years of glass research history is “crystallization”!

Surprisingly few studies about Li₂O-CaO-SiO₂ glasses have been published so far, despite the possibility of obtaining glass-ceramics displaying high strength and toughness. Previous works on this system include the identification of the crystalline phases and a

* Corresponding author.

E-mail address: giseleguis@gmail.com (G.G. Santos).

study of the ternary and pseudo-binary diagrams (Fig. 1) by A.R. West [6], a study of some properties and the influence of liquid phase separation, by J.E. Shelby and S.R. Shelby [7], and a study of the influence of the addition of certain components, such as MgO, SrO, Al₂O₃ and ZnO, on the properties of glass-ceramics, by S. M. Salman et al. [8–10].

More recently, some of us studied the kinetics of nucleation and crystallization of non-stoichiometric glasses of the Li₂SiO₃ – CaSiO₃ system [11]. Compositions containing 35, 47, 50, 60 and 66 mol% of CaSiO₃ were analyzed to determine their nucleation rates, crystal growth rates, crystal shape and size. Glasses containing 35 mol% of CaSiO₃ showed the highest nucleation rates among the studied compositions, whereas the nucleation rates decreased as the molar content of CaSiO₃ increased. In the second part of the paper [12], the same authors described the influence of the residual liquid composition on the crystallization process. They found that, because Ca ions are less mobile than Li ions, wollastonite crystallization is delayed compared to that of the lithium metasilicate phase in glasses of the LS-CS system. Consequently, only the formation of LS is observed in the initial stages of crystallization. This shifts the composition of the residual melt towards calcium metasilicate until the latter reaches the composition corresponding to the metastable liquidus temperature. LS crystals remain in equilibrium with the residual melt until CS crystals form by heterogeneous nucleation and growth, which again leads to changes in the composition of the residual liquid and the resumption of LS crystallization, until the material eventually crystallizes completely.

In this work, we study the microstructural development of Li₂O – CaO – SiO₂ glasses in response to heat treatments aimed at obtaining glass-ceramics containing elongated CaO·SiO₂ (wollastonite) or Li₂O·SiO₂ crystals inside the glass, without using nucleating agents. Calcium silicate glasses are known to have low nucleation rates and to undergo mostly surface crystallization [13]. On the other hand, pure lithium metasilicate (LS) glasses show extremely high nucleation rates (10²⁵ m⁻³ s⁻¹, according to the estimations by Fokin et al. [11]), which are comparable to values reported for some metallic alloys. In the current LS - CS glasses, lithium metasilicate nuclei form spontaneously in response to appropriate heat treatment, and remain embedded in the residual

glassy matrix with a composition approaching that of wollastonite during the growth of LS crystals [11,12]. Upon further heat treatment, the CaO-rich glassy matrix crystallizes around the lithium metasilicate crystals or at the LS/melt interphase, inducing internal crystallization of wollastonite. Therefore, both LS and CS crystals are formed inside the glass.

That being said, the core goal of this article is to explore the possibility of developing new CS-LS glass-ceramics with controlled microstructures, using the high spontaneous nucleation rates of lithium metasilicate to obtain a material with outstanding mechanical properties, such as high toughness, K_{IC}, and elastic modulus, E, due to the good mechanical properties of both wollastonite and LS.

2. Experimental

Compositions from 30 to 50 mol% of CaSiO₃ (the remainder consisting of Li₂SiO₃) were studied, more specifically formulations containing 32, 44 and 47 mol% of CaSiO₃ (47 mol% CaSiO₃ being the eutectic, according to Fig. 1). These compositions are hereinafter referred to as B32, B44 and B47, respectively. We chose to work within this compositional range because we believed it could generate crystallized samples with adequate combinations of the two crystal phases having good mechanical properties, while simultaneously maintaining reasonable internal nucleation rates without using a nucleating agent. This idea was based on our previous fundamental studies on the crystallization mechanism and kinetics of this system [11,12].

Calcium carbonate (98%, J. T. Baker), lithium carbonate (99%, Synth) and fumed silica (99.8%, Sigma-Aldrich) were weighed, mixed, deposited in an alumina crucible and subjected to a preheat treatment (800 °C for 20 h) to facilitate the release of carbon dioxide. The weights before and after the pretreatment were monitored. The mixed reagents were then fused in a platinum crucible at about 1400 °C, poured 3 times and remelted to promote homogenization, cast onto a flat steel plate and annealed at a temperature 60 °C below the T_g of each glass for 3–6 h.

Monolithic samples weighing about 20 mg were analyzed by DSC (differential scanning calorimetry, NETZSCH 404) at a heating

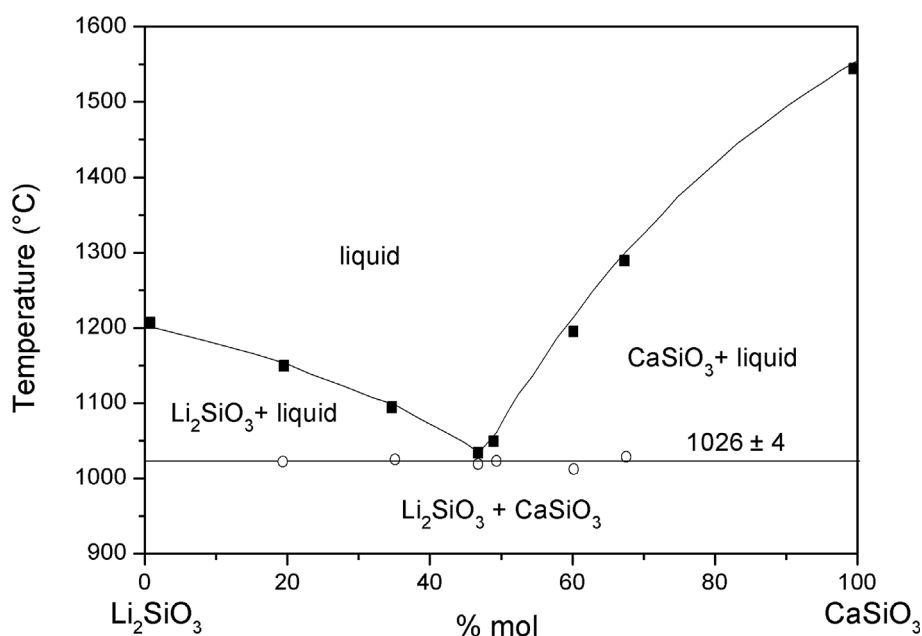


Fig. 1. Phase equilibrium diagram of the binary Li₂SiO₃ – CaSiO₃ system. The lines were taken from Ref. [6]; the data points were estimated from DSC curves in Ref. [11].

rate $q = 10\text{ }^{\circ}\text{C}/\text{min}$ up to $1100\text{ }^{\circ}\text{C}$ to determine the glass transition temperature (T_g), the temperatures of the crystallization peaks (T_c), etc.

The samples were then heat-treated in a homemade horizontal electrical furnace. The treatments were designed according to the DSC data, and the temperatures were monitored with previously calibrated chromel–alumel thermocouples. The furnace temperatures were within approximately $1\text{ }^{\circ}\text{C}$ of the chosen pre-set temperatures.

After the heat treatments, the microstructures of the glass-ceramic samples were analyzed. Specimens were polished and analyzed in a Leica DMRX optical microscope using a $50\text{--}100\times$ zoom. Samples exhibiting good mechanical properties and/or unusual mechanical behavior or microstructures were also analyzed by SEM (scanning electron microscopy) and by EDS (energy-dispersive x-ray spectroscopy) to obtain information about the distribution of the chemical constituents in different regions and thus gain a deeper understanding of their microstructures. Topography images of the fracture surfaces of the sample with the best mechanical properties were obtained using the Extended Depth of Field technique in a Nikon Eclipse LV100N POL microscope.

Samples crystallized at different temperatures were milled, reduced to $22\text{ }\mu\text{m}$ in size, and analyzed by X-ray diffraction (Ultima IV, Rigaku) in the following conditions: step-scan mode, $0.02^{\circ}/\text{step}$, 1 s counting time per step, and $\text{CuK}\alpha$ radiation ($\lambda_{\text{Cu}} = 1.5418\text{ \AA}$).

The distribution of phases (wollastonite, lithium metasilicate and residual glass) was estimated mainly based on image contrast, using Fiji software, since the lithium metasilicate crystals were easily distinguishable from the matrix. Analyses of the XRD patterns (peak height and area ratio between peaks and baseline) were also done as a complementary method and reasonable results were found.

The samples' hardness and indentation fracture toughness (K_C) were determined by means of Vickers indentation tests. All the samples were tested in a Future-Tech F7 hardness tester, applying a load of 5 N and 15 s of dwell time, using a Vickers diamond indenter. We used this approximate method to estimate K_C as a fast way to select the best candidate compositions and heat treatment conditions for the mechanical properties. Vickers hardness, H_V , was determined by Eq. (1) and the indentation fracture toughness, K_C , was determined by Eq. (2), as suggested by Niihara et al. [14], for Palmqvist type cracks:

$$H_V = 1.854 \left(\frac{p}{d^2} \right), \quad (1)$$

$$K_C = 0.035 \left(\frac{l}{a} \right)^{-\frac{1}{2}} \left(\frac{H_V}{E\Phi} \right)^{-\frac{2}{5}} \left(\frac{H_V a^{\frac{3}{2}}}{E\Phi} \right), \quad (2)$$

where p is the applied load, d is the average diagonal indentation, l is the crack length, a is the distance corresponding to half the impression produced by the indenter, E is the elastic modulus, and Φ is the restriction factor ($\cong 3$).

Instrumented indentation was also employed to evaluate the hardness and elastic modulus. The measurements were made using a XP™ Nanoindenter (MTS Instruments). At least 16 indentations were made under a maximum applied load of 400 mN in eight increasing loading/unloading cycles, using a Berkovich diamond indenter calibrated against a fused silica reference sample. The hardness and elastic modulus were calculated from the load and contact depth data, according to the Oliver and Pharr method [15].

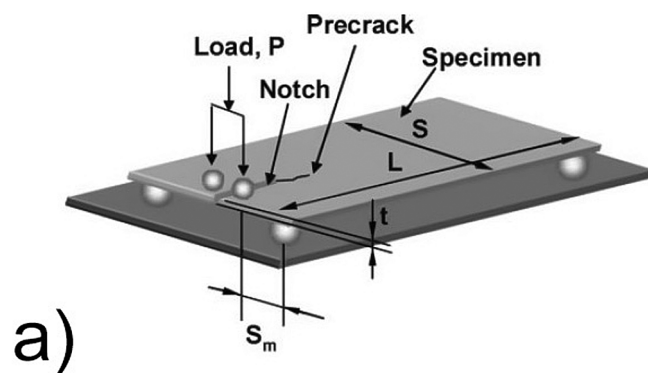
Finally, the composition yielding the best set of mechanical properties was analyzed by the ball-on-three-balls test (B3B) and double torsion technique to determine its mechanical strength σ_m

and fracture toughness, K_{DTIC} , respectively.

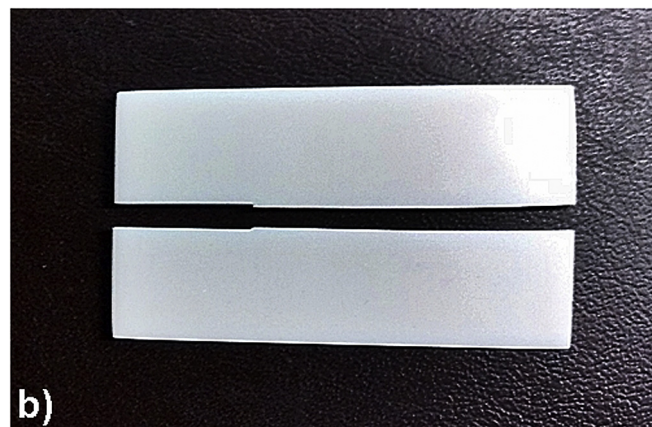
The mechanical strength of B44 samples were measured by the ball-on-three-balls tests [16]. The apparatus consists of 3 alumina spheres with 8 mm diameter under the sample within a certain distance so that each one touches the others. Another alumina sphere of the same size is centered on top of the sample. The tests were conducted in a 5 kN AGS-X Shimadzu universal mechanical testing machine with a compression rate of $500\text{ }\mu\text{m}/\text{min}$ at $23\text{ }^{\circ}\text{C}$ and 72% relative humidity. Five disk samples with 13 mm diameter and approximately 1.3 mm thick were prepared by grinding the glass-ceramic samples using SiC slurry followed by final polishing with a solution of water and CeO_2 . Before testing, all samples were annealed at $50\text{ }^{\circ}\text{C}$ below T_g for 2 h and slowly cooled for residual stress relief. The mechanical strength was calculated according to the equation of ref. [16] assuming a Poisson's ratio of 0.23 .

For K_{DTIC} measurement, five $15 \times 30 \times 1.5\text{ mm}^3$ samples were subjected to heat treatment for crystallization and then carefully polished. The samples were annealed at a temperature $50\text{ }^{\circ}\text{C}$ below their T_g for 2 h , after which a 10 mm long by 0.4 mm wide notch was created in the samples, using a diamond disk. After notching, a new annealing treatment (again $50\text{ }^{\circ}\text{C}$ below T_g for 2 h) was applied to alleviate any stresses introduced by the cutting operation and thus ensure the sample would fracture correctly. A detailed description of the experimental apparatus used here is given in Ref. [17]. The tests were performed in a universal testing machine (Shimadzu AGS-X 5 kN). The K_{DTIC} was determined as described in Refs. [18,19]:

$$K_{DTIC} = PS_m \left(\frac{3}{St^4(1-\nu)\psi} \right)^{1/2}, \quad (3)$$



a)



b)

Fig. 2. a) Schematic view of the double-torsion test apparatus and loading arrangement [19]; b) Example of a B44 sample fractured after a double-torsion test.

where P is the fracture load, ν is the Poisson ratio (~ 0.2), t is the sample thickness, S is the specimen width, S_m is the moment arm, and ψ is equal to $1 - 0.6302 \cdot \tau + 1.20 \cdot \tau \cdot \exp(-\pi/\tau)$, where $\tau = 2t/S$.

Fig. 2(a) show a schematic representation of the double-torsion specimen and 2(b) an example of a fractured sample after testing. When the fracture path deviated sideways from the straight path, the sample was not considered.

Residual stresses measurements around each crystalline phase was performed using X-ray diffraction at room temperature in the Bragg-Brentano geometry with a $\text{CuK}\alpha$ anode tube in an Ultima IV/Rigaku diffractometer of a bulk B44 glass-ceramic sample. A B44 glass-ceramic powder produced by grinding and sieved in a 50 μm metallic mesh was used as a stress free reference sample. The bulk sample was annealed at 50 $^\circ\text{C}$ below T_g for 2 h after polishing for residual stress relief produced during sample preparation. The recorded angular 2θ range was from 5 $^\circ$ to 100 $^\circ$ in 0.02 $^\circ$ steps with a 16s step scan. Rietveld refinement of the crystal structures was performed using the GSAS program [20] with the EXPGUI interface [21]. The average strains ϵ_i in each phase were calculated from the change of the cell parameters of each crystalline phase by comparing monolithic (stressed) and powder (stress free) samples [22–24] as $\Delta V/3V$, where ΔV is the difference between the crystal unit cell volumes V in the bulk and powder samples. The stress σ_{ri} in each phase i was obtained from Hooke's law as $\sigma_{ri} = E_i/(1 - 2\nu_i) \cdot \epsilon_i$.

3. Results

3.1. Differential scanning calorimetry – DSC

We studied three compositions of the $\text{Li}_2\text{O}-\text{CaO}-\text{SiO}_2$ system containing from 30 to 50 mol% of CaSiO_3 (the remainder being Li_2SiO_3). The three compositions showed similar DSC curves (Fig. 3) with two crystallization peaks. Both peaks shifted to higher temperatures with increasing CaSiO_3 content; the first peak being the most affected by these compositional changes. Table 1 shows the main characteristic temperatures for the three glasses under study. The glass transition temperatures were determined from the intersection of two tangent lines.

3.2. Identification of crystalline phases

Our samples differed in appearance, depending on the heat

Table 1

Data obtained from the DSC traces of the three compositions. T_{c1} and T_{c2} are related to the crystallization peak temperatures, while T_{solidus} was assigned to the beginning of the melting peaks.

	T_g ($^\circ\text{C}$)	T_{c1} ($^\circ\text{C}$)	T_{c2} ($^\circ\text{C}$)	T_{solidus} ($^\circ\text{C}$)
B32	450	560	680	1012
B44	470	634	705	1012
B47	478	680	707	1012

treatment they underwent. Fig. 4 illustrates the difference between the B44 samples treated at different crystal growth temperatures. The sample in the middle was subjected to crystal growth heat treatment at the temperature of the first crystallization peak, 634 $^\circ\text{C}$, for 2 h (according to the DSC trace in Fig. 3) and exhibited a translucent appearance, while the opaque sample on the right was treated at the beginning of the second crystallization peak, 700 $^\circ\text{C}$, for 2 h.

According to our XRD analyses, lithium metasilicate crystals and a residual glass phase coexist in the samples of compositions B32 and B44 treated at the first crystallization peak, T_{c1} . B44 and B47 already showed a small amount of wollastonite when treated at T_{c1} (Fig. 5). However, it is worth keeping in mind that the residual melt varies in each composition and that wollastonite crystallization is strongly dependent on temperature, so it is difficult to make a direct comparison of these XRD patterns. Samples treated at the beginning of the second peak showed wollastonite and lithium metasilicate (Fig. 6). A very small amount of a residual glass phase

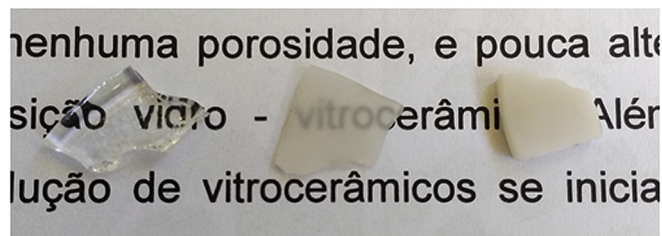


Fig. 4. Visual appearance of the B44 samples. Left: parent glass (no treatment); Middle: sample treated for 2 h at 634 $^\circ\text{C}$, i.e., first crystallization peak temperature (translucent); Right: sample treated for 2 h at 700 $^\circ\text{C}$, i.e., second crystallization peak temperature (opaque).

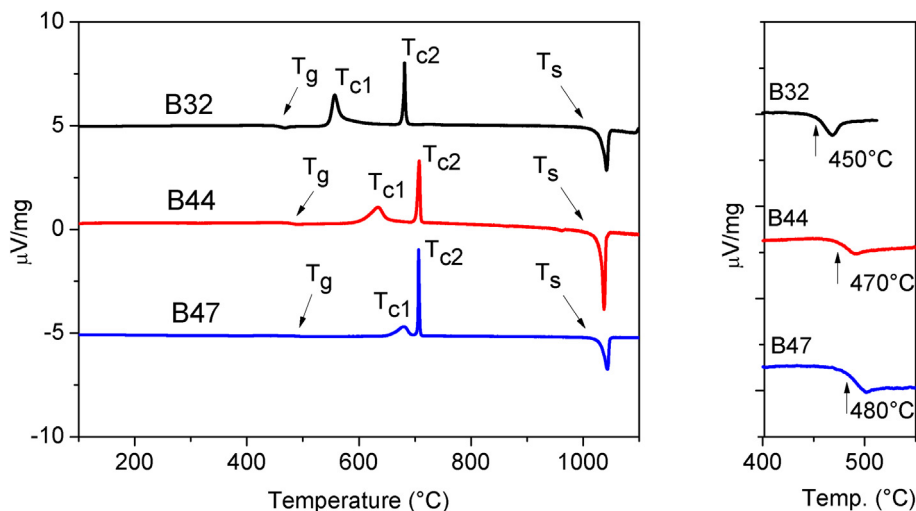


Fig. 3. DSC plots of the three compositions under study. The arrows indicate the glass transition temperatures, T_g .

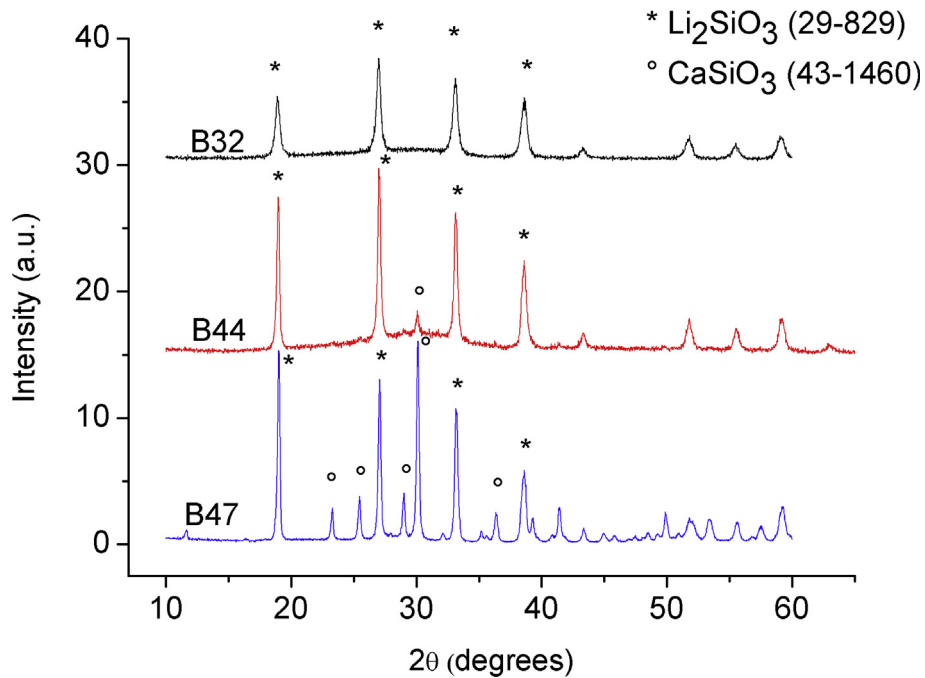


Fig. 5. Diffractograms of samples treated at the temperatures of the first crystallization peak. The heat treatments were: B32, nucleation at 470 °C for 5 min and crystal growth at 560 °C for 30 min; B44, nucleation at 498 °C for 24 h and crystal growth at 634 °C for 2 h; B47, nucleation at 508 °C for 24 h and 678 °C for 2 h. The numbers in brackets refer to the PDF card identification numbers.

was still present after treatment at the temperature corresponding to onset of the second peak (about 670 °C for compositions B32 and 700 °C for B44 and B47); these samples were highly (>75%) crystalline. Figs. 5 and 6 show X-ray diffractograms of samples of all the compositions heat-treated at the first and second crystallization peak temperatures.

3.3. Mechanical properties

Hardness, elastic modulus and fracture toughness were determined for several glass-ceramics developed in this work.

3.3.1. Vickers indentation tests

Hardness and indentation fracture toughness were measured by

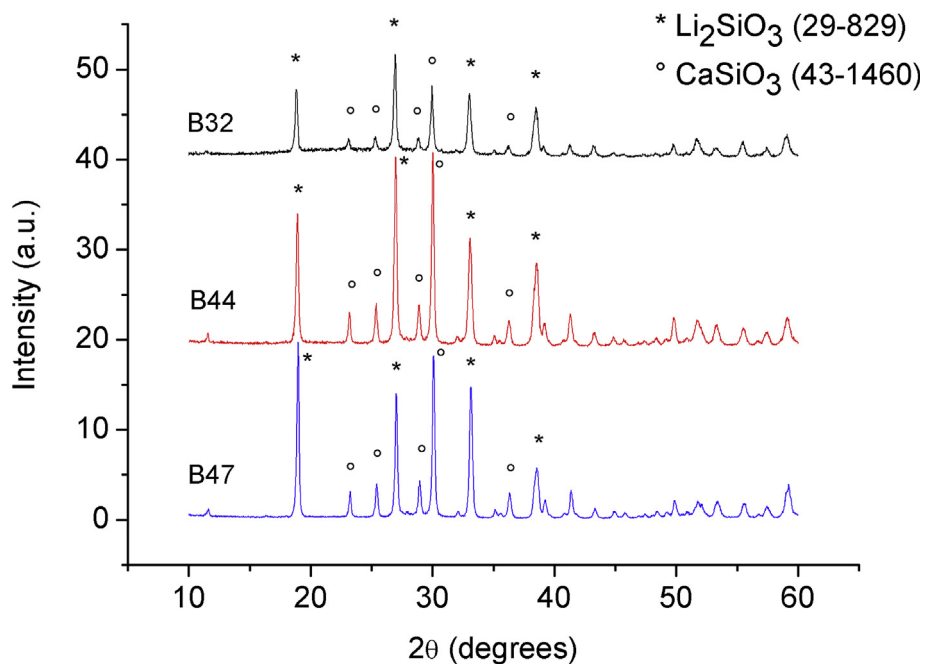


Fig. 6. Diffractograms of samples treated at the temperatures of the second crystallization peak. The heat treatments used were: B32, nucleation at 470 °C for 5 min and crystal growth at 670 °C for 2 h; B44, nucleation at 498 °C for 24 h and crystal growth at 700 °C for 2 h; B47, nucleation at 508 °C for 24 h and 700 °C for 2 h. The numbers in brackets correspond to PDF card identification numbers.

Vickers' indentation. We are fully aware of the limitations of indentation techniques in estimating fracture toughness [25]. We used this technique simply as a faster way to screen samples that displayed potentially good mechanical properties for further and more detailed characterization.

Table 2 describes the hardness and indentation fracture toughness calculated using Eqs. (1) and (2) (see the Introduction section). The volume fractions of each phase are also listed in Table 2; lithium metasilicate crystals were easily distinguishable in the glassy matrix, so the estimates were made by analysis of cross-sectional areas and complemented by XRD analysis (peak height and area ratio).

It was not possible to determine the indentation fracture toughness of all the B47 samples and the B44 sample subjected to a single heat treatment because the crack pattern obtained could not be monitored by the methods used in this work, as specified by ASTM C1327-08 [26]. Fig. 7 shows the two crack patterns found in this work: the expected pattern (Fig. 7a) and the one with random cracks around the indentation (Fig. 7b).

The hardness of the three glasses lies in the range of 6.6–7.0 GPa and their indentation fracture toughness is approximately $0.9 \text{ MPa m}^{1/2}$. It is noteworthy that the hardness increases slightly as the Ca content increases. All the compositions have the same average number of bridging oxygens/tetrahedron ($\text{BO} = 2$). Hardness is known to be sensitive to changes in the glass network and we believe that the substitution of Li_2O with CaO leads to more Ca^{2+} connecting two tetrahedra (while Li^+ can only connect to one NBO), which can increase the rigidity of the network; however, our data about the glass structure does not suffice for a more in-depth analysis.

Double heat treatments for nucleation and growth in the first crystallization peak (T_{c1}) resulted in a significant increase in hardness to 8.0 GPa for B32 and B44, and a moderate increase in indentation fracture toughness, to $1.1 \text{ MPa m}^{1/2}$ and $1.4 \text{ MPa m}^{1/2}$ (i.e., increases of 22 and 55%, respectively, relative to the parent glass). Heat treatments for crystal growth at the second crystallization peak (T_{c2}) significantly increased the indentation fracture toughness from ~ 0.9 to 1.8 and $2.2 \text{ MPa m}^{1/2}$ (for B32 and B44 compositions, respectively). However, the B47 glass-ceramics showed a decline in hardness compared to that of the parent glass in response to all the heat treatments. These experiments were double-checked and the results were confirmed. It should be noted that B44 and B47 show different indentation crack patterns (Fig. 7), but so far we have found no explanation for this behavior.

3.3.2. Hardness and elastic modulus

The data obtained by instrumented indentation are displayed in Fig. 8 and the hardness and elastic modulus at the maximum contact depth are listed in Table 3. Only the indentations with a contact depth greater than 600 nm were considered, since all the samples presented some surface roughness even after polishing with a $3 \mu\text{m}$ diamond suspension.

Once again, the best results – higher hardness and elastic modulus – were obtained for the B44 composition. However, considering the uncertainties of the measurements, it can be concluded that the B44 and B32 compositions showed similar H and E results.

3.3.3. Mechanical strength and fracture toughness

The double heat-treated B44 glass-ceramic exhibits the best mechanical properties among all the compositions under study and was chosen for the (time consuming) ball-on-three-balls and double-torsion tests to obtain its biaxial strength and fracture toughness. The average strength of the B44 was $270 \pm 20 \text{ MPa}$. Table 4 shows the measured values for fracture toughness by

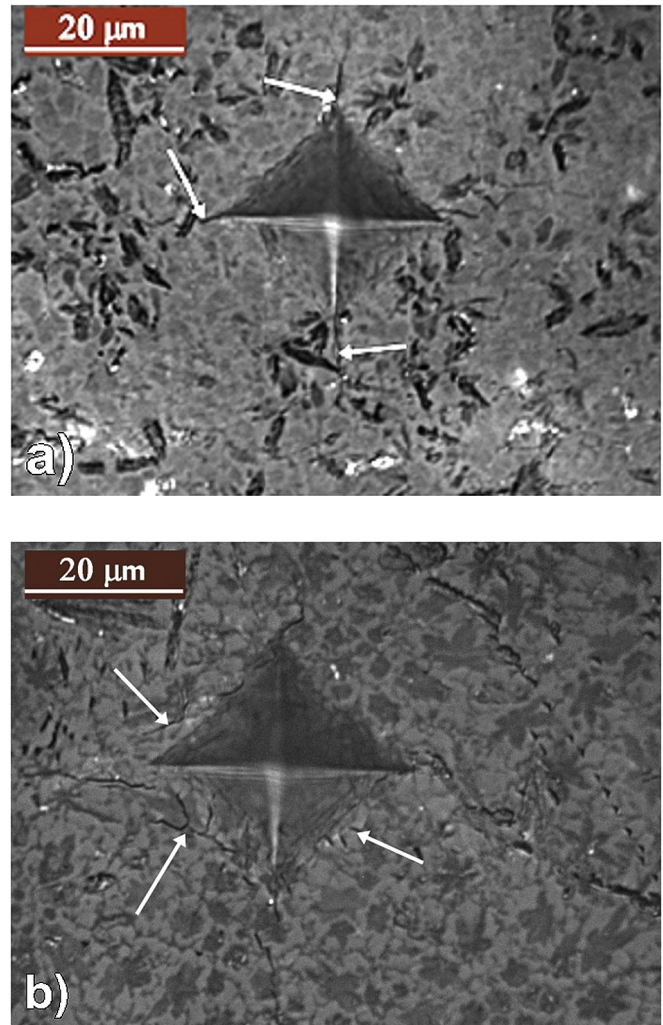


Fig. 7. Indentation crack patterns in a glass-ceramic containing CaSiO_3 and Li_2SiO_3 crystals obtained after heat-treating the parent glasses as follows: a) B44 – $498^\circ\text{C}/24 \text{ h}$ (nucleation) and $700^\circ\text{C}/2 \text{ h}$ (crystal growth); b) B47 – $508^\circ\text{C}/24 \text{ h}$ (nucleation) and $700^\circ\text{C}/2 \text{ h}$ (crystal growth). The arrows point to cracks around the indentations.

double torsion tests (K_{DTIC}).

The average K_{DTIC} of the best B44 glass-ceramic is therefore $(2.3 \pm 0.5) \text{ MPa.m}^{1/2}$. Its microstructure will be described in the next section.

3.3.4. Residual stress measurements

The unit cell volumes and the corresponding residual stresses on the wollastonite and lithium metasilicate phases in the B44 bulk glass-ceramic are presented in Table 5. The residual stress in the wollastonite crystals is $-138 \pm 8 \text{ MPa}$ (compressive) and is, surprisingly, almost null in the lithium metasilicate phase: $10 \pm 6 \text{ MPa}$.

3.4. Analysis of microstructure and chemical composition

3.4.1. Microstructural analysis by optical microscopy

The microstructural analysis was an important step of this study because it enabled us to correlate the mechanical properties of the glass-ceramics with the volume fraction of the crystalline phases, crystal sizes and shapes.

Fig. 9 shows micrographs of all the compositions, varying only the type of heat treatment: single or double. As expected, the crystallization pattern is strongly influenced by the type of heat

Table 2Heat treatment conditions, estimated volume fraction and H_V and K_C values determined by Vickers indentation tests of the compositions under study.

Composition	Heat treatment (nucleation/ growth)	H_V (GPa)	K_C (MPa.m ^{1/2})	Volume fraction% (estimated)
B32	Glass	6.6 ± 0.1	0.9 ± 0.1	–
	470°C/5 min and 560°C/30 min (crystal growth at T_{c1})	8.0 ± 0.1	1.0 ± 0.1	40% glass 60% LS 0% CS
	470°C/5 min and 670°C/2 h (crystal growth at T_{c2})	7.0 ± 0.1	1.8 ± 0.1	24% glass 53% LS 23% CS
	670°C/2 h (only crystal growth at T_{c2})	7.3 ± 0.1	1.4 ± 0.1	29% glass 53% LS 18% CS
B44	Glass	6.9 ± 0.2	0.9 ± 0.1	–
	498°C/24 h and 634°C/2 h (crystal growth at T_{c1})	8.0 ± 0.2	1.4 ± 0.1	28% glass 53% LS 19% CS
	498°C/24 h and 700°C/2 h (Crystal growth at T_{c2})	7.8 ± 0.2	2.2 ± 0.1	14% glass 54% LS 32% CS
	700°C/2 h (only crystal growth at T_{c2})	6.7 ± 0.1	–	19% glass 53% LS 28% CS
B47	Glass	7.0 ± 0.2	1.0 ± 0.1	–
	508°C/24 h and 673°C/2 h (crystal growth at T_{c1})	5.1 ± 0.1	–	21% glass 50% LS 29% CS
	508°C/24 h and 700°C/2 h (crystal growth at T_{c2})	5.0 ± 0.3	–	16% glass 52% LS 32% CS
	700°C/2 h (only crystal growth at T_{c2})	5.5 ± 0.1	–	21% glass 50% LS 29% CS

treatment, the only exception being composition B32, although its crystallization pattern is similar in both cases. On the other hand, the B44 and B47 samples subjected to a single heat treatment exhibit larger crystals than those that underwent double heat treatment. The reason for this disparity may be the nucleation rate of these glasses. The B44 and B47 glasses exhibit lower nucleation rates than the B32, indicating that a single heat treatment naturally generates a smaller number of nuclei and, hence, has a stronger effect on the final microstructure.

The average size of the lithium metasilicate crystals in compositions B32 and B44 subjected to double heat treatments is approximately 8.5 μm (Fig. 9b and d). Note that the samples with larger crystals (B44 single heat treatment, B47 single and double heat treatment; Fig. 9 c, e and f, respectively) were those whose K_C could not be measured by indentation. Moreover, composition B47 presented the lowest values of hardness and elastic modulus, as shown in Fig. 8 and Tables 2 and 3. We will discuss our assumptions about these behaviors later in the Discussion section.

3.4.2. Microstructural and chemical analysis by SEM and EDS

The samples displaying the best mechanical properties and/or with unusual microstructures (i.e., microstructures that deviate from those commonly found in this work) were evaluated by SEM and EDS. Fig. 10 shows the microstructure of composition B44. Three different regions were observed: a “flower-like” structure (A) with acicular crystals approximately 7 μm long x 2 μm thick, several polyhedra (B) with plane faces and a hexagonal morphology 1 μm in diameter, and a lighter matrix (C) in which they were both immersed. These images portray cross-sections of the sample; therefore, several polyhedra could be in different sections of the “flower’s” beam.

We also evaluated the chemical compositions in different regions of the samples by EDS. Table 6 lists the concentration of calcium present in each region.

The B47 sample was also analyzed. Fig. 11 shows the resulting micrographs.

Once again, the EDS analyses indicate the amount of calcium in regions A and C (Table 7). The B47 sample did not show two types of crystal morphology, so the determinations were done only in region A, the flower-like crystal, and C, the white region.

Lithium could not be detected due to its low atomic mass. In addition, the irradiated spots are always larger than the actual crystals. Nevertheless, taking into account the result of XRD analysis, we attribute the black areas and the white regions around them to lithium and calcium metasilicate crystals, respectively. Moreover, electron back scattering is stronger in the case of heavy elements, i.e., light colored sites correspond to Ca-rich regions. These results therefore confirm that wollastonite can be crystallized inside a sample after the initial crystallization of lithium metasilicate.

Fig. 12 shows the fracture surface of the B44 sample subjected to double heat treatment, using secondary (left) and backscattered electrons (right) in SEM. The fracture surface is rough, revealing a substantial amount of crack deflection. Large portions of the fracture surface consist of flat surfaces, and a comparison with the backscattered image indicates that they correspond to the cleavage of lithium metasilicate crystals. Fig. 13 shows the fracture surface topography obtained by EDF (Extended Depth of Field) microscopy. The sample’s surface roughness varies from 5 to 10 μm , which is similar to the average size of lithium metasilicate crystals found in the B32 and B44 samples (8.5 μm).

4. Discussion

As mentioned earlier, only glasses containing 30–50 mol% of CaSiO_3 were studied. Glasses containing more than 50% CaSiO_3 showed only surface crystallization of wollastonite, which could impair the mechanical performance of the samples. In addition,

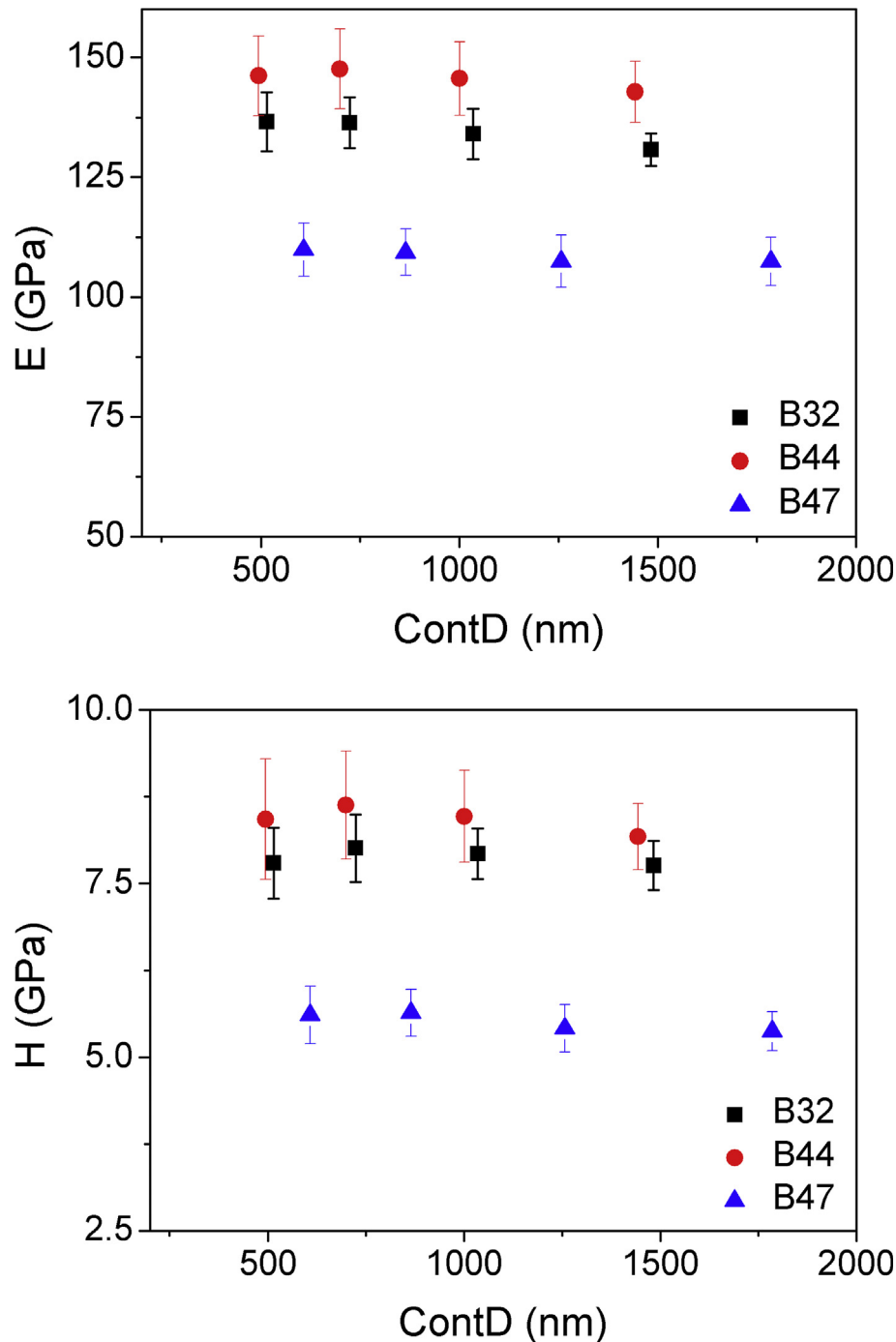


Fig. 8. Comparison of hardness and elastic modulus of B32, B44 and B47 glass-ceramics as a function of contact depth. E and H were determined using a Berkovich indenter. The heat treatment conditions are the same as those shown in Table 2 at T_{c2} (double heat treatment).

samples with high CaSiO_3 content show significantly lower (practically undetectable) nucleation rates (lower homogeneous nucleation of LS), which implies longer nucleation treatment times. As was shown in Refs. [11,12], increasing the CS content causes the homogeneous volume nucleation of LS to decrease significantly, and the glasses containing more than 50 mol% of CS exhibited only surface nucleation, predominantly of CS crystals. This decrease in the nucleation rate is the reason for the following observation: to obtain micron-sized crystals in B32 glass, the nucleation treatment was performed for 5 min, whereas 24 h were needed to obtain a similar result in the B44 composition (see Fig. 9).

Based on the sequence of crystalline phases (LS and CS) studied in detail in Refs. [11,12] and corroborated by the present work, it can be concluded that LS crystals serve as active sites for the nucleation of wollastonite that crystallizes around them. Therefore, the LS-crystal/melt interface or the enrichment of the residual melt composition by calcium, or both, could trigger the nucleation of wollastonite. In short, LS crystals play the role of “nucleating agents.” It should be kept in mind that a second heat treatment must be performed at T_{c2} to accelerate the formation of CS crystals.

Among the three evaluated compositions, B44 (44 mol% of CaSiO_3) exhibited the best mechanical properties – higher

Table 3

Hardness and elastic modulus of the best glass-ceramics of each composition, determined by nanoindentation at the maximum contact depth, using a Berkovich indenter. The heat treatment conditions are the same as those shown in Table 2 at T_{c2} (double heat treatment). These nanohardness values are compatible with the microhardness values listed in Table 2.

Composition	H (GPa)	E (GPa)
B32	7.8 ± 0.4	131 ± 3
B44	8.2 ± 0.5	143 ± 6
B47	5.4 ± 0.3	107 ± 5

Table 4

Fracture toughness of composition B44 determined by double torsion tests.

Sample	Thickness (mm)	Width (mm)	Fracture load (N)	K_{DTIC} (MPa.m ^{1/2})
1	1.5	15	54.7	2.3
2	1.7	15	73.3	2.3
3	1.5	15	61.4	2.4

Table 5

Unit cell volumes and residual stresses in each crystalline phase of composition B44 glass-ceramic determined by XRD.

Phase	Sample	Unit cell volume (Å ³)	Residual stress (MPa)
wollastonite	powder	795.07 ± 0.06	-138 ± 8
	bulk	794.00 ± 0.06	
Lithium metasilicate	powder	237.95 ± 0.02	10 ± 6
	bulk	237.99 ± 0.02	

hardness, elastic modulus and indentation fracture toughness. This behavior can be explained by considering the other compositions. In other words, based on the results (Fig. 8 and Table 3), we can state that the presence of CaSiO₃ crystals in this system gives it better mechanical properties (notably fracture toughness) than the Li₂SiO₃ crystalline phase combined with residual glass (obtained by crystal growth heat treatment at T_{c1}).

It can therefore be concluded that composition B32 does not exhibit better mechanical properties than B44, given the lower CaSiO₃ content in the former. For instance, for glass-ceramics of the MgO-CaO-SiO₂-P₂O₅ system, Kobuko and coworkers [27] reported that the crystallization of wollastonite results in considerably improved bending strength, elastic modulus (~120 GPa) and fracture toughness (2.0–2.6 MPa m^{1/2}). This was attributed to the relatively high fracture surface energy of wollastonite due to crack deviation from a straight path. The system studied by Kobuko et al. does not contain Li₂SiO₃, but their results substantiate the idea that the wollastonite phase in glass-ceramics leads to good toughness.

The B47 glass-ceramic presents lower hardness and elastic modulus than the compositions with smaller wollastonite content, such as B32 and B44 glass-ceramics. We believe that one reason for this is microcracking caused by the significant difference between the thermal expansion coefficients of the two crystalline phases. The thermal expansion coefficients, TEC, of CaSiO₃ and Li₂SiO₃ are $\alpha_W = 6 \times 10^{-6} \text{ }^\circ\text{C}^{-1}$ [28] and $\alpha_{LM} = 15 \times 10^{-6} \text{ }^\circ\text{C}^{-1}$ [29], respectively. Although the TEC mismatch does not directly affect hardness and elastic modulus, microcracking such as that visible in the B47 samples shown in Fig. 14 may do so. Previous studies [11] have shown that microcracking of lithium metasilicate crystals occurs even before crystallization of the wollastonite phase in the same B47 composition. This can also be explained by the difference in the coefficients of thermal expansion of lithium metasilicate crystals and the glass matrix. The α of the B47 glass was estimated using SciGlass software, and was found to be $11 \times 10^{-6} \text{ K}^{-1}$ for the parent glass, disregarding the presence of crystalline phases. It is

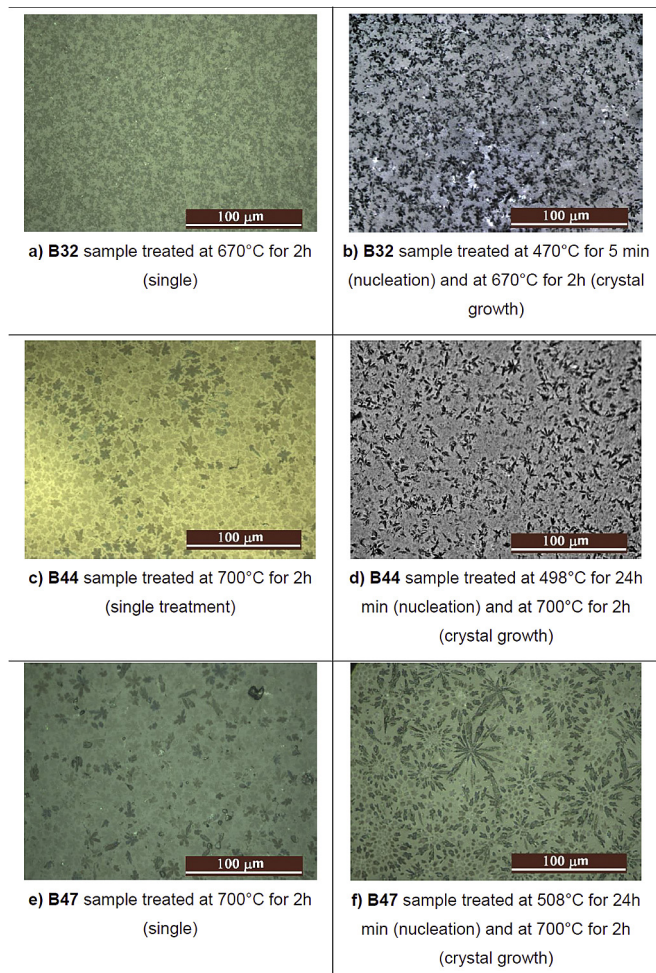


Fig. 9. Optical micrographs of the three compositions subjected to single and double heat treatment. The compositions and heat treatment conditions are specified under each image.

noteworthy that as the lithium metasilicate crystals are formed first, the glass matrix becomes richer in calcium metasilicate [12], which further decreases its TEC and increases the discrepancy between the α values of the crystal phase and residual glass.

Fig. 15 also shows that composition B47 has a higher surface “porosity” content than compositions B32 and B44. The effect of this porosity on hardness will be discussed later.

The apparently larger amount of microcracking in composition B47 can probably be attributed to three factors: (i) different thermal expansion coefficients of the wollastonite, glass and lithium metasilicate phases, (ii) crystal size, and (iii) different volume fractions of wollastonite.

The first factor is the mismatch between thermal expansion coefficients and how this mismatch can explain the crack behavior in the crystal/matrix system. To simplify our calculations we will consider lithium metasilicate crystals as the precipitate and wollastonite as a homogeneous matrix. According to Selsing’s model for residual stresses in glass-ceramics [30], the stresses are tensile in the precipitate when its thermal expansion coefficient is higher than that of the matrix. Therefore, the matrix is subjected to tensile radial stresses and compressive tangential stresses, and cracks are expected to deviate from the precipitates [24]. However, the cracks induced by indentation did not exhibit this behavior (as can be seen in Fig. 7 a), and in most cases the cracks propagated

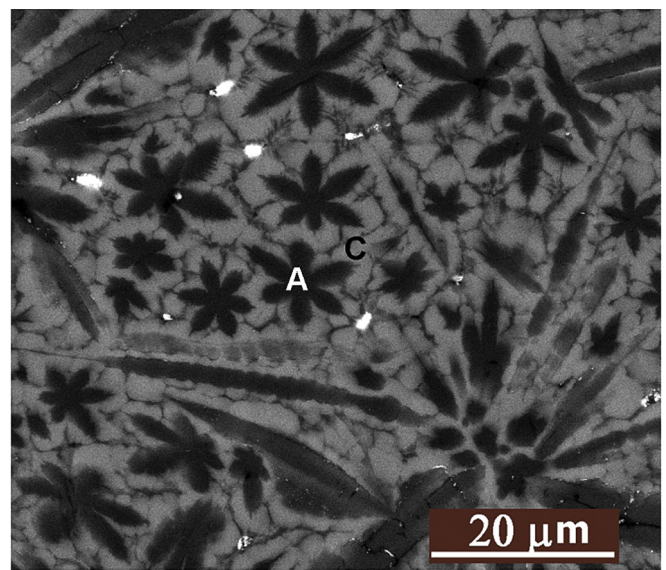
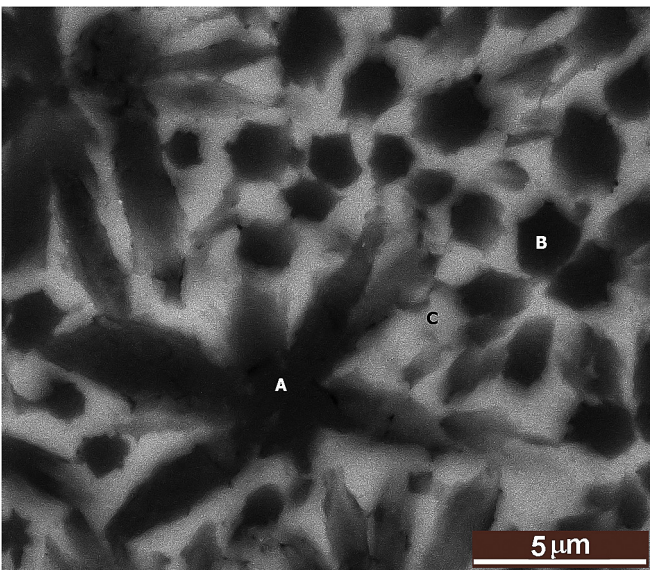
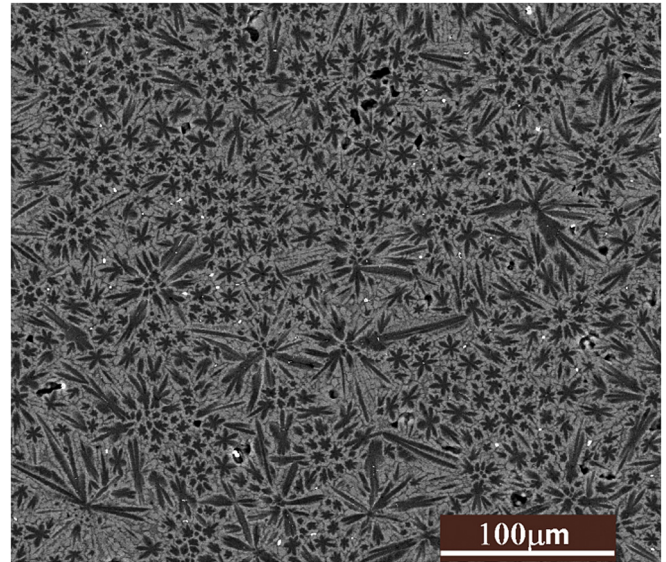
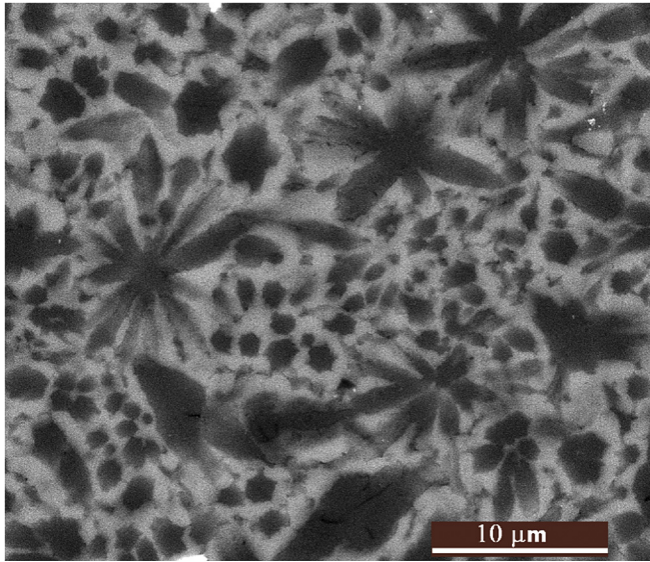


Fig. 10. SEM BSE (backscattered electrons) images of the B44 sample heat-treated at 498°C/24 h (nucleation) and 700°C/2 h (crystal growth). This is the same sample shown in Fig. 9d.

Fig. 11. SEM BSE images of B47 samples heat-treated at 508°C/24 h (nucleation) and 700°C/2 h (crystal growth). This is the sample shown in Fig. 9f.

inside the lithium metasilicate crystals (Fig. 14).

The stresses inside lithium metasilicate crystals can be estimated. As their shape is acicular, we estimated them using the expressions deduced by Hsueh and Becher [31] for the residual stresses inside a fiber-shaped inclusion. The stresses σ_3 along the fiber length and σ_1 and σ_2 in the directions perpendicular to the fiber length are:

$$\sigma_1 = \sigma_2 = A \left[\left(\frac{(1 + \nu_{LS})}{E_{LS}} + \frac{f(1 + \nu_W)}{(1 - f)E_W} \right) \right] \Delta\alpha \cdot \Delta T \quad (4)$$

$$\sigma_3 = A \left[\left(\frac{(1 + \nu_{LS})}{E_{LS}} + \frac{(2 + f)}{(1 - f)E_W} \right) \right] \Delta\alpha \cdot \Delta T \quad (5)$$

where A is a constant given by:

$$A = \left[\left(\frac{(1 + \nu_{LS})(1 - 2\nu_{LS})}{E_{LS}^2} + \frac{f(2 - \nu_{LS} - \nu_W - 4\nu_{LS}\nu_W) + 1 + \nu_W}{(1 - f)E_{LS}E_W} + \frac{f(1 + \nu_W)(1 + f - 2f\nu_W)}{(1 - f)^2 E_W^2} \right) \right]^{-1} \quad (6)$$

Table 6

Approximate percentages of calcium present in different spots of Fig. 10.

Region	Ca (weight %)
A (flowerlike)	5
B (hexagons)	9
C (white)	15

Table 7

Approximate percentages of calcium found in different spots in Fig. 11.

Region	Ca (% weight)
A (flowers)	4
C (white)	17

$\Delta\alpha$ is the thermal expansion mismatch between the wollastonite and lithium metasilicate phases, ΔT is the temperature range in which the stresses develop (we will consider ΔT as the difference

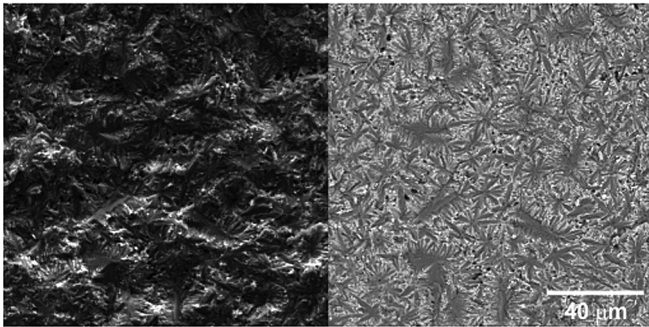


Fig. 12. SEM micrographs of fracture surfaces of a B44 sample treated at 498°C/24 h and 700°C/2 h, using secondary electrons (left image) and backscattered electrons (right image).

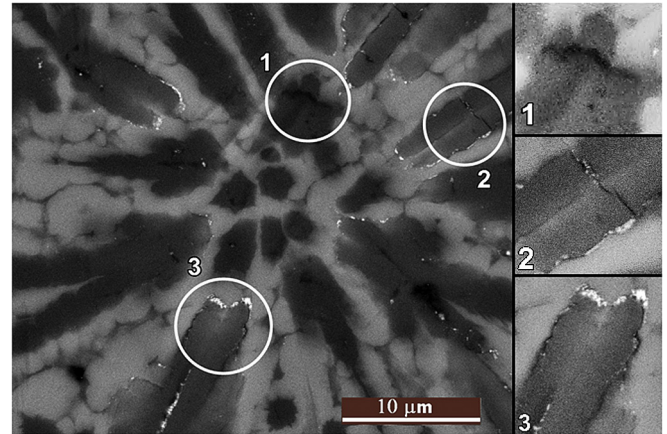


Fig. 14. SEM micrograph of a B47 glass-ceramic. The circles show microcracking inside lithium metasilicate crystals.

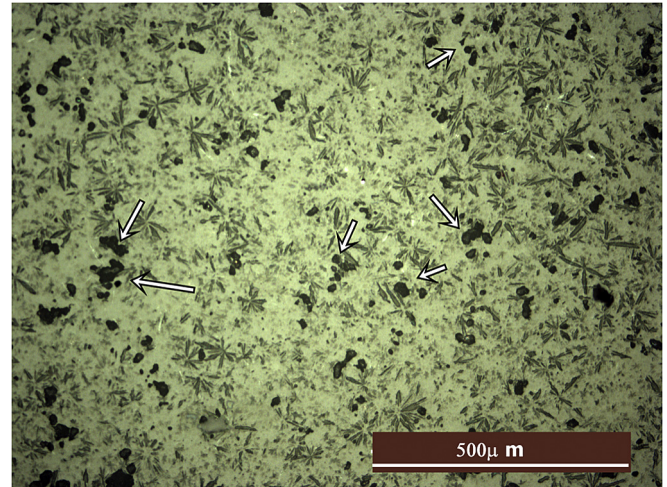


Fig. 15. Optical micrograph of a B47 surface sample treated at 508°C/24 h for nucleation and 700°C/2 h for crystal growth. The white arrows indicate porosity.

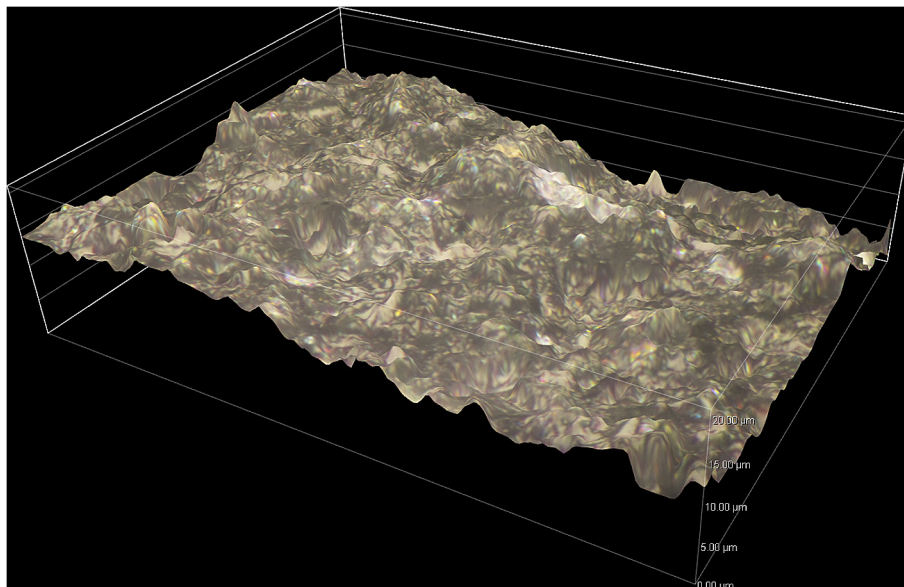


Fig. 13. Fracture surface topography of the B44 sample (treated at 498°C/24 h and 700°C/2 h) obtained by EDF microscopy.

between T_g and room temperature), f is the volume fraction of inclusions, E is the elastic modulus, ν is Poisson's ratio, and the subscripts W and LS refer to wollastonite and lithium metasilicate, respectively. Assuming $E_{LS} = 120$ GPa, $\nu_{LS} = 0.2$ [32], $E_W = 130$ GPa, $\nu_W = 0.29$ [33], $T_g = 470$ °C and $f = 0.60$ (average lithium metasilicate content in the three compositions) and considering a fully crystallized material, we obtain $\sigma_1 = \sigma_2 = 147$ MPa and $\sigma_3 = 390$ MPa. The higher residual stress occurs in the direction of the lithium metasilicate acicular crystals and is tensile. Therefore, if microcracking occurs, it is expected to be perpendicular to the dendrite arms. The average residual stress in the wollastonite matrix can be estimated using Newton's third law. Considering an average metasilicate stress as $\bar{\sigma}_{LS} = (\sigma_1 + \sigma_2 + \sigma_3)/3$, the average stress in wollastonite is:

$$\bar{\sigma}_w = -\frac{f\bar{\sigma}_{LS}}{(1-f)} \quad (7)$$

Based on the above calculated data, the average stress in metasilicate crystals is 228 MPa (tensile), and based on Eq. (7), the average stress in wollastonite is -341 MPa (compressive). Therefore, should cracking occur in the microstructure, it is expected to do so in the metasilicate acicular crystals. This is indeed observed, as illustrated in detail in Fig. 14.

The same steps can be used to estimate residual stresses in two other limiting situations of interest: i) the case in which all the lithium metasilicate crystallizes and the residual melt composition is that of wollastonite; and ii) the case of the B47 composition at $T = 675$ °C, studied by Fokin et al. [12], in which the crystallization of lithium metasilicate is arrested when the melt composition containing 75 mol% of CS reaches equilibrium (the melt composition can be determined by T_g).

In the first situation, considering a general composition of $30\text{Li}_2\text{SiO}_3 \cdot 20\text{CaSiO}_3 \cdot 50\text{SiO}_2$ ($f_{LS} = 0.6$), after all the lithium metasilicate crystallizes, a composition of $\text{Li}_2\text{O} \cdot \text{SiO}_2$ is predicted for the

crystallized phase and of $\text{CaO} \cdot \text{SiO}_2$ for the glass matrix. Using Eqs. (4)–(7) and SciGlass software to estimate the TEC, E and Poisson's ratio for the melt ($\nu_{\text{melt}(w)} = 0.27$, $E_{\text{melt}(w)} = 89$ MPa, $\alpha_{\text{melt}(w)} = 8.2 \times 10^{-6} \text{ K}^{-1}$), we obtained the following results for the residual stresses:

$$\begin{aligned} \sigma_{LS} (\text{average}) &= 116 \text{ MPa} \\ \sigma_{\text{melt}(w)} (\text{average}) &= -174 \text{ MPa} \end{aligned}$$

Compared to the first estimate ($\sigma_{LS} = 228$ MPa and $\sigma_W = -341$ MPa), which considers a fully crystallized material, we can confirm that the crystallization of a second phase (wollastonite) increases the residual stresses.

In the second situation, Fokin et al. [12] defined the melt composition for a B47 sample treated at 675 °C as containing 75 mol % of CS. In this case, the compositions of the crystalline phase and melt are approximately $20\text{Li}_2\text{O} \cdot 20\text{SiO}_2$ and $23\text{CaO} \cdot 7\text{Li}_2\text{O} \cdot 30\text{SiO}_2$, respectively. Once again, using SciGlass software and Eqs. (4)–(7), we obtained $\nu_{\text{melt}} = 0.27$, $E_{\text{melt}} = 94$ MPa, $\alpha_{\text{melt}} = 9 \times 10^{-6} \text{ K}^{-1}$ and the following values of stresses:

$$\begin{aligned} \sigma_{LS} (\text{average}) &= 158 \text{ MPa} \\ \sigma_{\text{melt}} (\text{average}) &= -236 \text{ MPa} \end{aligned}$$

A comparison of all these values of residual stresses reveals the evolution of residual stresses in the system as the phases (LS and CS) crystallize.

The second factor that can influence microcracking is crystal size. Spontaneous cracking occurs when a minimum critical crystal size is reached, above which the stored elastic energy is sufficient to create fresh crack surfaces [22–24]. As can be observed in Fig. 7a and b, the metasilicate crystals of B47 samples are larger than those of B44 samples, indicating a higher probability of microcracking in the former.

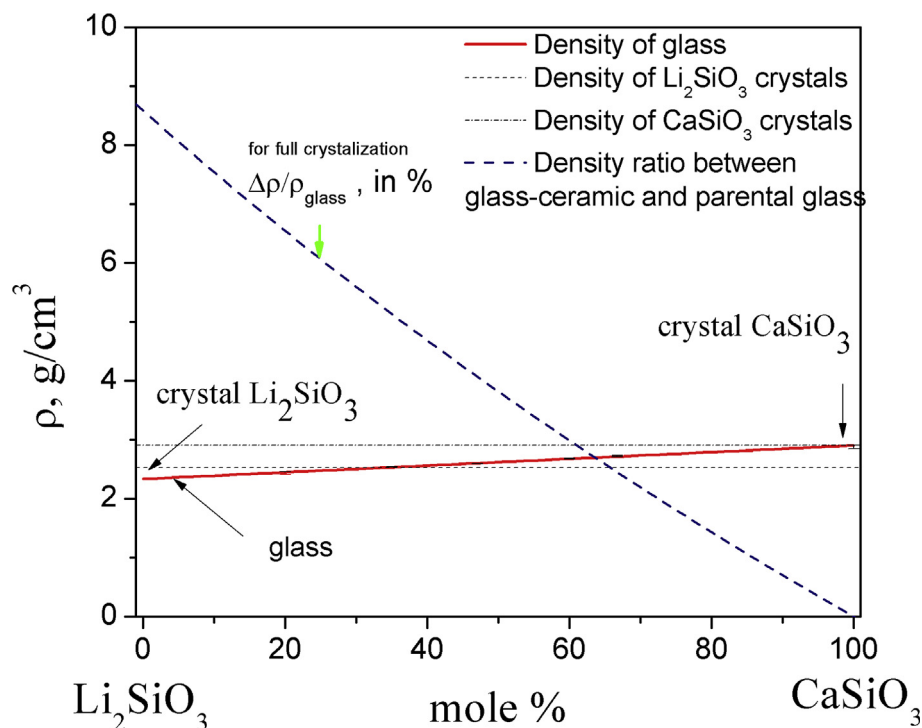


Fig. 16. Glass density according to composition in the Li_2O - CaO - SiO_2 system (adapted from Ref. [11]). $\Delta\rho$ is the difference between the density of fully crystallized glass and that of a parent glass.

The third factor that contributes to the greater probability of microcracking in B47 samples is the volume fraction of wollastonite. From Eq. (7), one can infer that a higher wollastonite volume fraction in B47 samples induces higher residual tensile stresses in the metasilicate crystals, when compared with the B44 sample. Therefore, higher tensile stress promotes more microcracking of the lithium metasilicate crystals.

Another physical property that affects microcracking is fracture toughness. When the thermal expansion of precipitates is higher than that of the matrix, microcracking can occur inside the precipitate if its fracture toughness, K_{IC} , is lower than that of the matrix [24]. In other words, microcracking inside lithium metasilicate crystals can be explained by a lower K_{IC} in comparison to the wollastonite crystalline phase. At present, we do not know the experimental fracture toughness of pure wollastonite and lithium metasilicate crystals, but based on our observations, this is likely the case of the studied compositions.

Comparison of the calculated residual stresses with the experimental values measured by XRD presented in Table 5 reveal a lower (than predicted) value of the experimental residual stresses around wollastonite and almost no residual stress in the lithium metasilicate phase. This can be readily explained by stress relief due to microcracking of the lithium metasilicate crystals. The residual stress in the LS crystals is almost completely relieved with a consequent decrease in the wollastonite crystals. This phenomenon has been observed previously by us in a photothermal refractive glass-ceramics [23].

Another explanation for the lower hardness and elastic modulus of B47 samples when compared to B44 samples is their higher porosity. It is known that porosity decreases the elastic modulus of ceramics [34]. Its effect is very marked, even at low levels of porosity, because an exponential relation of the form $E = E_0 \exp(-bP)$ seems to describe well this relationship [34], where E is the elastic modulus affected by porosity, E_0 is the elastic modulus with no porosity, P is the porosity ($0 < P < 1$) and b is a constant ($3 < b < 5$). The effect of porosity on hardness follows a similar relationship, since it limits the elastic recovery of the indents, and is especially remarkable at lower loads (< 10 N) [35,36]. Luo and Stevens studied the dependence of the elastic modulus and hardness on porosity in yttria-stabilized zirconia having different degrees of porosity [37]. They found that E and H are exponentially dependent on porosity, and that the effect is strong even at low values of porosity. For example, 10% of porosity reduces the values of E and H by approximately 25% when compared to the E and H of a pore-free sample. Therefore, even a slight increase in porosity of the B47 samples over that of the B44 samples may also explain their lower H and E values.

Porosity can be formed in glass-ceramics as a way to offset the elastic strains resulting from differences in the density of glass and crystalline phases [38]. However, as Fig. 16 shows, there is a strong suggestion that the density mismatch between parent glass and fully crystallized glass samples decreases as the wollastonite content increases. Accordingly, the B47 glass-ceramics samples, which have the highest wollastonite content, should exhibit lower porosity than the B32 and B44 samples.

Another general cause for porosity in glass-ceramics is the release of gases (e.g., O_2 and CO_2) due to the difference in their solubility in the glass and crystals. Some gases that are soluble in glasses are likely less soluble in the newly formed crystallized phases; therefore, some of these gases may be released in the liquid in the form of bubbles during the crystallization process above T_g . The microstructure of the B47 glass-ceramic differs slightly from the B32 and B44 microstructures, having larger crystals distributed in a different manner. This is likely the reason for the porosity found in some samples.

As for compositions and mechanical properties, in the B44 composition, the proportion between the two crystalline phases was close to ideal for optimum mechanical behavior. Given its superior mechanical properties, we choose to perform the time consuming double-torsion tests on these samples, and the result was $K_{DTIC} = 2.3 \pm 0.5$ MPa $m^{1/2}$. Fig. 12 reveals a rough fracture surface due to crack deflection by the crystals. Crack deflection is considered one of the predominant toughening mechanisms in ceramics [39]. In the Li_2O - CaO - SiO_2 glass-ceramic with 44 mol% of $CaSiO_3$, this mechanism is important because of the presence of lithium metasilicate crystals. It produces a large cleavage area, usually at large deflection angles. Both aspects are important for energy dissipation during crack propagation. These mechanical properties are already relatively high for glass-ceramics, but could possibly still be improved upon further optimization of the heat treatments and resulting microstructures.

5. Conclusions

We demonstrated that it is possible to obtain crystalline wollastonite in the interior of Li_2O - CaO - SiO_2 glasses without using external nucleating agents. This is because lithium metasilicate (LS) crystals act as “nucleating agent” in this system. LS crystals initially precipitate by homogeneous nucleation, after which the wollastonite crystallizes in the Ca-rich glass phase around the LS.

The measured residual stresses around wollastonite and lithium silicate crystals are smaller than the theoretical values due to microcracking.

The toughness of samples containing both lithium metasilicate and wollastonite dispersed in a residual glass is superior to that of glassy specimens and of samples containing only lithium metasilicate and a residual glass. Among the studied compositions, B44 (containing 44 mol% of $CaSiO_3$) showed the best combination of hardness, 8.2 ± 0.5 , and elastic modulus, $E = 146 \pm 8$ GPa. For this reason, the B44 glass-ceramic was subjected to double torsion tests, which yielded $K_{DTIC} = 2.3 \pm 0.5$ MPa $m^{1/2}$. The average fracture strength of this glass-ceramic was 270 ± 20 MPa. These mechanical properties have not yet been fully optimized but are higher than those of most glass-ceramics.

Acknowledgments

The authors thank Dr. Ivan Mathias for performing the K_{DTIC} double torsion tests, Dr. C. M. Lepienski for the use of his nano-indenter, and C-LABMU/UEPG/FINEP/CAPES/Fundação Araucária for the use of the SEM-FEG. We are also grateful to FAPESP – the São Paulo Research Foundation (Process no. 2013/07793-6) and to CAPES – Brazil’s Federal Agency for the Support and Improvement of Higher Education, for their financial support of this research.

References

- [1] J.E. Shelby, *Introduction to Glass Science and Technology*, second ed., The Royal Society of Chemistry, 2005.
- [2] T. Berthier, V.M. Fokin, E.D. Zanotto, New large grain, highly crystalline, transparent glass-ceramics, *J. Non-Cryst. Solids* 354 (2008) 1721–1730.
- [3] G. Beall, *Design and properties of glass-ceramics*, *Annu. Rev. Mater. Sci.* 22 (1992) 91–119.
- [4] M. Montazerian, S.P. Singh, E.D. Zanotto, An analysis of glass-ceramic research and commercialization, *Am. Ceram. Soc. Bull.* 94 (2015) 30–35.
- [5] J.C. Mauro, E.D. Zanotto, Two centuries of glass research: historical trends, current status, and grand challenges for the future, *Int. J. Appl. Glass. Sci.* 5 (2014) 313–327.
- [6] A.R. West, Phase equilibria in the system $Li_2O - CaO - SiO_2$, *J. Am. Ceram. Soc.* 61 (1978) 152–155.
- [7] J.E. Shelby, S.R. Shelby, Phase separation and the properties of lithium calcium silicate glasses, *Phys. Chem. Glas.* 41 (2000) 59–64.
- [8] S.M. Saliman, H. Darwish, E.A. Mahdy, Crystallization characteristics and physico-chemical properties of the glasses based on Li_2O - CaO - SiO_2 eutectic

- (954 °C) system containing magnesium oxide, *Ceram. Int.* 34 (2008) 1819–1828.
- [9] S.M. Salman, S.N. Salama, H.A. Abo-Mosallam, Crystallization behavior and properties of multicomponent strontium-containing Lithia calcia silicate glasses, *Ceram. Int.* 36 (2010) 2307–2314.
- [10] S.M. Salman, H. Darwish, E.A. Mahdy, The influence of Al₂O₃, MgO and ZnO on the crystallization characteristics and properties of lithium calcium silicate glasses and glass-ceramics, *Mater. Chem. Phys.* 112 (2008) 945–953.
- [11] V.M. Fokin, R.M.C.V. Reis, A.S. Abyzov, C.R. Chinaglia, E.D. Zanotto, Non-stoichiometric crystallization of lithium metasilicate–calcium metasilicate glasses. Part 1 — crystal nucleation and growth rates, *J. Non-Cryst. Solids* 362 (2013) 56–64.
- [12] V.M. Fokin, R.M.C.V. Reis, A.S. Abyzov, C.R. Chinaglia, J.W.P. Schmelzer, E.D. Zanotto, Non-stoichiometric crystallization of lithium metasilicate–calcium metasilicate glasses. Part 2 — effect of the residual liquid, *J. Non-Cryst. Solids* 379 (2013) 131–144.
- [13] L. Granasy, T. Wang, P. James, Kinetics of wollastonite nucleation in CaO.SiO₂ glass, *J. Chem. Phys.* 108 (1998) 7317–7326.
- [14] K. Niihara, R. Morena, D.P.H. Hasselman, Evaluation of K_{1c} of brittle solids by the indentation method with low crack-to-indent ratios, *J. Mater. Sci. Lett.* 1 (1982) 13–16.
- [15] W.C. Oliver, G.M. Pharr, An improved technique for determining hardness and elastic modulus using load and displacement sensing indentation experiments, *J. Mater. Res.* 7 (1992) 1564–1583.
- [16] A. Börger, P. Supancic, R. Danzer, The ball on three balls test for strength testing of brittle discs: stress distribution in the disc, *J. Eur. Ceram. Soc.* 22 (2002) 1425–1436.
- [17] F.C. Serbena, I. Mathias, C.E. Foerster, E.D. Zanotto, Crystallization toughening of a model glass-ceramic, *Acta Mater.* 86 (2015) 216–228.
- [18] D. Williams, A. Evans, A simple method for studying slow crack growth, *J. Test. Eval.* 7 (1974) 44–50.
- [19] A. Shyam, E. Lara-Curzio, The double-torsion testing technique for determination of fracture toughness and slow crack growth behavior of material: a review, *J. Mater. Sci.* 41 (2006) 4093–4104.
- [20] A.C. Larson, R.B. Von Dreele, General Structure Analysis System (GSAS), Los Alamos National Laboratory Report LAUR, 2000, pp. 86–748.
- [21] B.H. Toby, EXPGUI, a graphical user interface for GSAS, *J. Appl. Cryst.* 34 (2001) 210–213.
- [22] F.C. Serbena, V.O. Soares, O. Peitl, H. Pinto, R. Muccillo, E.D. Zanotto, Internal residual stresses in sintered and commercial low Expansion Li₂O–Al₂O₃–SiO₂ glass–ceramics, *J. Am. Ceram. Soc.* 94 (2011) 1206–1214.
- [23] F.C. Serbena, G.P. Souza, E.D. Zanotto, J. Lumeau, L. Glebova, L.B. Glebov, Internal residual stresses in partially crystallized photo-thermo-refractive glass, *J. Am. Ceram. Soc.* 94 (2011) 671–674.
- [24] F.C. Serbena, E.D. Zanotto, Internal residual stresses in glass-ceramics: a review, *J. Non-Cryst. Solids* 358 (2012) 975–984.
- [25] G.D. Quinn, R.C. Bradt, On the Vickers indentation fracture toughness test, *J. Am. Ceram. Soc.* 90 (2007) 673–680.
- [26] American Society for Testing and Materials (ASTM), C1327–08: Standard Test Method for Vickers Indentation Hardness of Advanced Ceramics, 2008.
- [27] T. Kobuko, S. Ito, M. Shigematsu, S. Sakka, T. Yamamuro, Mechanical properties of a new type of apatite-containing glass ceramic for prosthetic application, *J. Mater. Sci.* 20 (1985) 2001–2004.
- [28] G.R. Rigby, G.B.H. Loverr, A.T. Green, The reversible thermal expansion and other properties of some calcium ferrous silicates, *Trans. Br. Ceram. Soc.* 44 (1945) 37–52.
- [29] M.O.C. Villas-Boas, Desenvolvimento e caracterização de vitrocerâmicas do Sistema Li₂O–2SiO₂ para aplicação odontológica (PhD Thesis), Federal University of São Carlos, UFSCar, 2013 (in Portuguese).
- [30] J. Selsing, Internal stresses in ceramics, *J. Am. Ceram. Soc.* 44 (1961) 419.
- [31] C.H. Hsueh, P.F. Becher, Residual thermal stresses in ceramic composites. Part I: ellipsoidal inclusions, *Mater. Sci. Eng. A* 212 (1996) 22–28.
- [32] T. Tang, D.L. Luo, Density functional theory study of electronic structures in lithium silicates: Li₂SiO₃ and Li₄SiO₄, *J. At. Mol. Sci.* 1 (2010) 185–200.
- [33] C.C. Lin, K.S. Leung, P. Shen, S.F. Chen, Elasticity and structure of the compounds in the wollastonite (CaSiO₃)-Na₂SiO₃ system: from amorphous to crystalline state, *J. Mater. Sci. Mater. Med.* 26 (2015) article: 39.
- [34] W.D. Kingery, H.K. Bowen, D.R. Uhlmann, Introduction to Ceramics, second ed., Wiley-Interscience, 1976.
- [35] W. Lo, A.M. Campbell, Indentation-induced deformation and microcracking of highly textured superconducting (Bi,Pb) Sr₂Ca₂Cu₃O_x ceramic, *J. Mater. Res.* 10 (1995) 568–577.
- [36] J. Adachi, K. Kurosaki, M. Uno, S. Yamanaka, Porosity influence on the mechanical properties of polycrystalline zirconium nitride ceramics, *J. Nucl. Mater.* 358 (2006) 106–110.
- [37] J. Luo, R. Stevens, Porosity-dependence of elastic moduli and hardness of 3Y-TZP ceramics, *Ceram. Int.* 25 (1999) 281–286.
- [38] V.M. Fokin, A.S. Abyzov, J.W.P. Schmelzer, E.D. Zanotto, Stress induced pore formation and phase selection in a crystallizing stretched glass, *J. Non-Cryst. Solids* 356 (2010) 1679–1688.
- [39] K.T. Faber, A.G. Evans, Crack deflection processes — I. Theory, *Acta Metall.* 31 (1983) 565–576.